

All-Electrostatic Valley Filtering by Barrier Rotation in Tilted Dirac/Weyl Semimetals

Can Yesilyurt^{*1}

¹Nanoelectronics Research Center, Istanbul, Turkey

March 4, 2026

Abstract

Charge carriers in Dirac/Weyl semimetals with tilted anisotropic energy dispersion exhibit valley-dependent refraction and reflection at electrostatic barrier interfaces. Here, we show that an angled barrier interface provides a purely electrostatic route to valley filtering, producing finite valley-polarized conductance. We develop a generalized transfer-matrix formalism for the tilted, anisotropic Dirac Hamiltonian, extended to treat electrostatic barriers at arbitrary angles, and calculate the transmission in the rotated-barrier frame. We also present simulated valley-resolved trajectories in a finite device geometry, which clearly show that one valley is selectively transmitted, whereas the other is predominantly reflected by the angled barrier, without secondary effects such as real or pseudo-magnetic fields.

I. INTRODUCTION

Charge carriers in two-dimensional (2D) Dirac materials may carry a valley isospin degree of freedom, in addition to their real spin and charge [1, 2, 3]. The valley index labels the degenerate but inequivalent K and K' Dirac points in momentum space, and has emerged as a promising carrier of information for *valleytronics* [1, 3]. Generating and controlling valley-polarized currents requires breaking the degeneracy between the two valleys and then selectively filtering the transmission of one valley over the other [1, 2]. A considerable amount of effort has been devoted to achieving valley-dependent tunneling in condensed-matter systems. Valley polarization has been demonstrated by using magnetic fields [4, 5, 6], optical helicity [28], and line defects [1, 29]. One possible avenue is applying uniaxial strain to induce a relative shift of the two valleys in momentum space; as a result, electrons around different valleys experience refractions in opposite directions at the interface between strained and unstrained regions [30]. Although the gradient of uniaxial strain results in the angular separation of electron trajectories according to the valley index, this in itself would not give rise to valley-polarized conductance since the contributions

*canyesil@nanorescenter.com; can-yesilyurt@hotmail.com

of both valleys to the overall conductance remain identical. To induce a valley-polarized transport, one needs to break the angular symmetry of the transmission profile by means of transverse Lorentz displacement, which may be achieved by applying a magnetic barrier [31, 32, 33, 34]. However, each of these approaches presents practical limitations. External magnetic fields reduce practicability, ferromagnetic layers increase fabrication complexity and limit tunability, strain engineering necessitates nanoscale mechanical control, and line defects require atomic precision. Additionally, modulating valley polarization would require either altering the direction of the applied strain or switching the magnetization direction.

A qualitatively different avenue has opened with the discovery of tilted anisotropic semimetallic materials [12]. In these systems, the energy dispersion acquires a tilt term that gives rise to elliptic Fermi surface contours, which are displaced in opposite transverse directions for the two valleys in the presence of an electrical potential gradient [12, 16]. It has been previously shown that Weyl fermions that encounter a potential barrier experience an anomalous transverse momentum shift along the direction of the tilt [35, 36], and that this chirality-dependent refraction at the barrier interface polarizes the Weyl fermions in angle-space according to their valley index [17]. When an electrostatic potential V_0 is applied to form a barrier, the Fermi surface in the barrier region is mismatched with respect to the free region, and this mismatch can affect the two valleys oppositely due to crystal symmetry in materials hosting Dirac/Weyl fermions with tilted dispersion [15, 14]. This broad and growing class of tilted Dirac materials includes the semimetallic transition metal tellurides WTe_2 and MoTe_2 [24, 25], 8- $Pm\bar{m}n$ borophene [9, 10, 11], the organic conductor α -(BEDT-TTF) $2\text{I}3$ [12], $1T'$ -transition metal dichalcogenides [13], and strained graphene variants [12]. Among these, WTe_2 stands out as a particularly promising platform: its anisotropic energy dispersion has been experimentally confirmed [27, 26]. The tilt has profound consequences for Klein tunneling [37]: it has been shown that perfect transmission rotates to a finite *oblique Klein tunneling angle* θ_K , which is a material constant independent of energy and barrier height [15, 14]. Crucially, when the two valleys are tilted in opposite directions, the Klein tunneling peaks occur at $+\theta_K$ for the K valley and $-\theta_K$ for K' , which breaks the valley degeneracy in angle-space [15, 16]. It has previously been shown that this asymmetry, combined with a magnetic barrier configuration, can produce electrically controllable, switchable valley polarization in Weyl semimetals with tilted energy dispersion [17]. The asymmetric Klein tunneling has been further characterized in tilted Dirac cone systems [18], resonant transport in double-barrier tilted Dirac structures has been investigated [19], and a tunneling valley Hall effect driven by Fermi-surface mismatch has been predicted [20], arising purely from the tilt without Berry curvature.

It is now well established that the tilt-induced valley splitting in angle-space, combined with an appropriate symmetry-breaking mechanism, can produce net valley polarization [15, 16, 20]. Previously reported theoretical works consider transport through infinite planar junctions parameterized by a single conserved transverse momentum. In contrast, practical devices have finite channel widths, which allow carriers reflected at barrier interfaces to scatter off channel walls and subsequently re-encounter the barrier at modified angles. Furthermore, the influence of specific device geometry, such as angled potential barriers, as well as the combined effects of barrier angle,

barrier height, and finite dimensions on filtering efficiency, remains unaddressed.

Here, we show that an angled electrostatic gate on a tilted Dirac material can generate valley-polarized currents without the need for magnetic fields or strain engineering. We develop a generalized transfer-matrix formalism for the tilted anisotropic Dirac Hamiltonian, extended to treat barriers at arbitrary angles α relative to the transport direction. We further develop a semiclassical trajectory simulation in the full 2D device geometry, and directly demonstrates that the angled gate selectively transmits one valley while reflecting the other, thereby enabling valley filtering rather than merely valley separation. We apply this framework to 8-*Pmmn* borophene *n-p-n* junctions as a concrete example and show that the barrier angle α converts the intrinsic tunneling asymmetry into a net valley-polarized conductance, which is gate-tunable through the barrier height V_0 . The mechanism is general and applies to any material hosting tilted Dirac or Weyl cones, e.g., WTe₂, where anisotropic transport has been experimentally confirmed [27, 26]. The proposed device geometry [Fig. 1] features a single top gate positioned on a transport channel oriented at an angle α . The barrier height V_0 is continuously tunable, allowing precise electrostatic control over the resulting valley polarization.

II. DEVICE GEOMETRY AND MODEL

The proposed valley filter device is shown in Fig. 1. The device consists of a tilted Dirac material channel (e.g., 8-*Pmmn* borophene or few-layer WTe₂ flake) with source and drain contacts, a global back gate that sets the Fermi energy E_F , and a tilted top gate that defines an angled electrostatic barrier of height V_0 , as illustrated in Fig. 1 (a). The barrier region (shaded blue) is tilted by angle α relative to the y -axis, as shown in Fig. 1 (c) and (d). The energy-band diagram along the transport direction is depicted in Fig. 1 (b), where the tilted Dirac cones in the barrier region are shifted by V_0 relative to those in the free region.

The physical mechanism of the valley filter can be understood intuitively from the schematic diagrams in Fig. 1 (c) and (d). For a straight barrier ($\alpha = 0$), shown in Fig. 1 (c), the K (blue, dotted) and K' (red, dotted) carriers refract symmetrically upon entering the barrier, with the oblique Klein tunneling angle θ splitting them in opposite transverse directions. However, this angular separation does not produce net valley polarization in the integrated conductance, since the transmission profile is sampled symmetrically over all incident angles. When the barrier is tilted by $\alpha = 20^\circ$, as shown in Fig. 1 (d), the geometry breaks this symmetry: one valley (here K , thick blue dashed) encounters the barrier near its oblique Klein tunneling peak and transmits efficiently in a straight path, while the other valley (K' , red dotted) approaches at unfavorable angles and thus reflected from the barrier interface. This is the key mechanism: the barrier angle α converts the intrinsic angular splitting θ_K into a net valley-dependent conductance.

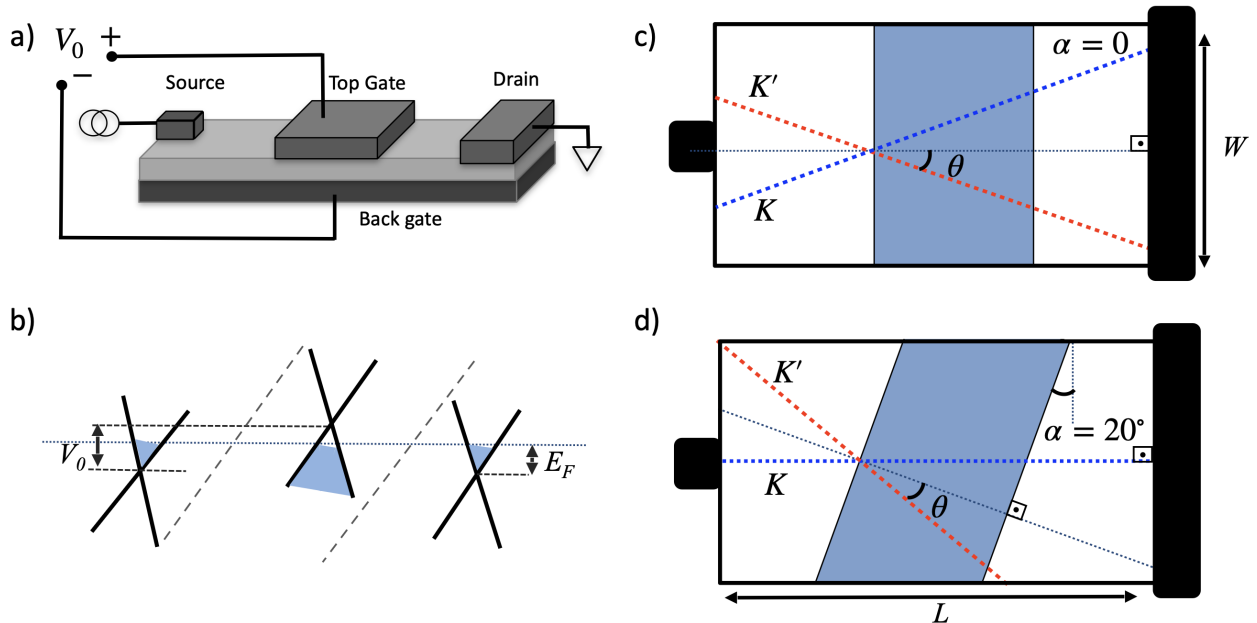


Figure 1: Proposed valley filter device and operating principle. (a) Three-terminal device schematic with source and drain contacts, a global back gate, and a tilted top gate defining the angled barrier of height V_0 . (b) Energy-band diagram along the transport direction showing tilted Dirac cones in each region; the barrier region cones are shifted by V_0 and the Fermi energy E_F is indicated. (c) Top-view illustration of the device with a straight barrier ($\alpha = 0$): K (blue, dotted) and K' (red, dotted) carriers refract symmetrically at the oblique Klein tunneling angle θ , producing no net valley polarization in the integrated conductance. (d) Tilted barrier ($\alpha = 20^\circ$): the angled barrier selectively transmits one valley while reflecting the other, giving rise to valley-polarized conductance.

A. Hamiltonian and energy dispersion

The low-energy quasiparticles near a single Dirac or Weyl point in a tilted anisotropic 2D material can be described by a general low-energy Hamiltonian [12, 11, 14]

$$H = \hbar v_x \sigma_x k_x + \hbar v_y \sigma_y k_y + \hbar s (w_x k_x + w_y k_y) \mathbb{I} + V(\mathbf{r}), \mathbb{I}, \quad (1)$$

where $\sigma_{x,y}$ are Pauli matrices acting on the sublattice pseudospin, $V(\mathbf{r})$ is the external electrostatic potential, v_x and v_y are anisotropic Fermi velocities along the transport (x) and transverse (y) directions, and w_x and w_y are tilt velocity components. The sign $s = \pm 1$ carries the valley index; in many tilted Dirac/Weyl materials, the two inequivalent valleys are tilted in opposite directions due to the underlying crystal symmetry (often linked to broken inversion symmetry), but this is not a universal rule, and multi-valley systems can host more complex tilt patterns. The type-I regime (i.e., closed Fermi surface) requires that the tilt magnitude remain smaller than the cone velocities; for a general tilt direction, this corresponds to $\sqrt{w_x^2/v_x^2 + w_y^2/v_y^2} < 1$. Solving the Hamiltonian in Eq. (1), the eigenvalues are found as

$$E_\lambda(\mathbf{k}) = V + \hbar s (w_x k_x + w_y k_y) + \lambda \sqrt{(\hbar v_x k_x)^2 + (\hbar v_y k_y)^2}, \quad (2)$$

with $\lambda = \pm 1$ the band index. Note that the pseudospin texture is determined solely by the anisotropic Dirac velocities v_x and v_y , while the tilt enters only through the identity matrix. This decoupling means the tilt rigidly displaces the Fermi contour without altering the chiral

structure [16]. For compactness we report velocity parameters in units of $v_F = 10^6 \text{ m s}^{-1}$ (e.g., $v_x = 0.86, v_F$), while $v_x, v_y, w_x,$ and w_y remain dimensional velocities. For the numerical calculations presented below, we use parameters representative of 8- $Pmmn$ borophene: $v_x/v_F = 0.86,$ $v_y/v_F = 0.69,$ with a transverse tilt of magnitude $|w|/v_F = 0.32$ directed along the y -axis ($\phi_t = 90^\circ$), giving a tilt ratio $\eta^2 = w_y^2/v_y^2 \approx 0.215$ (here $w_x = 0,$ so the tilt is purely transverse) [9, 11, 14].

The Hamiltonian in Eq. (1) is general and applies beyond the specific material parameters used here. An important case is WTe_2 , whose highly tilted, anisotropic low-energy dispersion has been experimentally confirmed at room temperature [27, 26], making it a promising candidate for the valley filtering scheme proposed here (see Sec. 4.3 for a detailed discussion of experimental prospects). The calculations presented below use 8- $Pmmn$ borophene parameters as a concrete example, but the valley filtering mechanism applies to any type-I tilted Dirac system.

For a straight barrier ($\alpha = 0$), translational invariance along the y -direction conserves k_y . In the presence of transverse tilt ($w_y \neq 0$), the direction of perfect transmission shifts to a finite oblique Klein tunneling angle $\theta_K \neq 0$ [15, 14]. When the two valleys are tilted in opposite directions, the transmission peaks appear at $+\theta_K$ for the K valley and $-\theta_K$ for K' , breaking the valley degeneracy in angle-space [15, 16].

We consider a one-dimensional rectangular potential barrier rotated by angle α relative to the y -axis, as illustrated in Fig. 1 (b) and (d), where the conserved quantum number in the barrier frame is $k_{\parallel} = k_x \sin \alpha + k_y \cos \alpha$. The barrier potential is described by $V(x, y) = V_0, \Theta(x_{\text{eff}}), \Theta(d - x_{\text{eff}})$, where $x_{\text{eff}} = x - y \tan \alpha$ is the barrier-frame coordinate (i.e., the x -intercept of the tilted barrier line through point (x, y)), d is the barrier width measured along x at $y = 0$, and Θ is the Heaviside step function. The effective barrier width perpendicular to the interface is $d_{\text{eff}} = d \cos \alpha$, which enters the transfer-matrix phase accumulation. The gradient of this potential produces a transverse force $F_y = -\partial V/\partial y = \tan \alpha; dV/dx_{\text{eff}}$ at each interface, which is absent for a straight barrier. In the semiclassical picture, this force imparts a transverse momentum shift $\Delta k_y \propto \tan \alpha$ at each barrier interface. The geometric rotation shifts the angular window of incidence equally for both valleys; because the two valleys refract on opposite sides of the tilted interface, the same angular shift moves one valley closer to its high-transmission (oblique Klein) direction while moving the other away, as illustrated schematically in Fig. 1 (c) and (d).

III. RESULTS

A. Valley-dependent conductance

The total valley-dependent conductance can be calculated considering the anisotropic band dispersion based on the Landauer–Buttiker formalism [22]. The valley-resolved ballistic conductance is given by

$$G_s = G_0 \frac{W}{2\pi} \int_{k_y^-(s)}^{k_y^+(s)} T(E, k_y; s) \frac{v_x^{\text{grp}}(k_y, s)}{v_F} dk_y, \quad (3)$$

where $G_0 = 4e^2/h$ is the conductance quantum (including spin and valley degeneracies), W is the channel width, and $v_x^{\text{grp}} = w_x s + \lambda v_x^2 k_x / \sqrt{(v_x k_x)^2 + (v_y k_y)^2}$ is the x -component of the

anisotropic group velocity [14, 22]. The integration limits $k_y^\pm(s)$ correspond to the boundaries of the propagating-mode window, which are determined by requiring k_x to be real in the free region. For $\alpha \neq 0$, the transmission T in Eq. (3) is evaluated using the conserved tangential momentum k_\parallel from Sec. 4.1, while the integration remains over the transverse modes k_y of the free region (i.e., the incoming channel modes at the source contact).

To demonstrate the efficiency of the all-electrical valley-filter device, the proposed model is evaluated using material parameters for 8-*Pmmn* borophene, and the conductance G/G_0 is calculated as a function of the electrostatic potential V_0 . In Fig. 2 (a), the conductance G/G_0 as a function of V_0 is given for a straight barrier ($\alpha = 0^\circ$) device geometry (i.e., schematically illustrated in Fig. 2 (e)). The four calculated curves corresponding to the K and K' valleys for both the transfer-matrix method and the semiclassical approach are presented. For each method, the K and K' curves lie on top of each other, confirming that a straight barrier does not produce net valley polarization, i.e., consistent with previously published theoretical predictions [14, 15]. The TMM and semiclassical results are in close agreement: in the *n-p-n* regime ($V_0 > E_F$), the Fabry-P'erot oscillations differ between the two methods because the finite channel width introduces wall reflections, as shown in the trajectory plots (see Fig. 3). This leads to trapped resonant modes at the barrier interfaces, which can either enhance or suppress conductance oscillations.

The valley degenerate conductance profile changes qualitatively when the barrier is tilted. Figure 2 (b) shows the conductance for $\alpha = 20^\circ$, with the corresponding device geometry shown in Fig. 2 (d). Below $V_0 \approx E_F$, the curves remain approximately degenerate. However, above $V_0 \approx E_F$, all four curves become clearly distinguishable: the K -valley conductance (both TMM and semiclassical) remains high, while the K' -valley conductance drops substantially, as indicated by the arrows in Fig. 2 (b). Within each valley, the TMM and semiclassical results track each other closely, with the semiclassical oscillations again somewhat smoothed by the finite device geometry. This valley-dependent conductance splitting is the central result of this work. The splitting onset coincides with the transition from *n-n'-n* to *n-p-n* transport (i.e., when the barrier Dirac point crosses E_F), which is the regime where the Fermi surface mismatch between two regions is more pronounced. [15, 14]. Similarly, the valley-dependent conductance difference $\Delta G/G_0 = (G_K - G_{K'})/G_0$ is shown in Fig. 2 (c), where the ΔG is approximately zero for $V_0 < E_F$ and grows to values of order $\Delta G/G_0 \sim 5-6$ in the *n-p-n* regime.

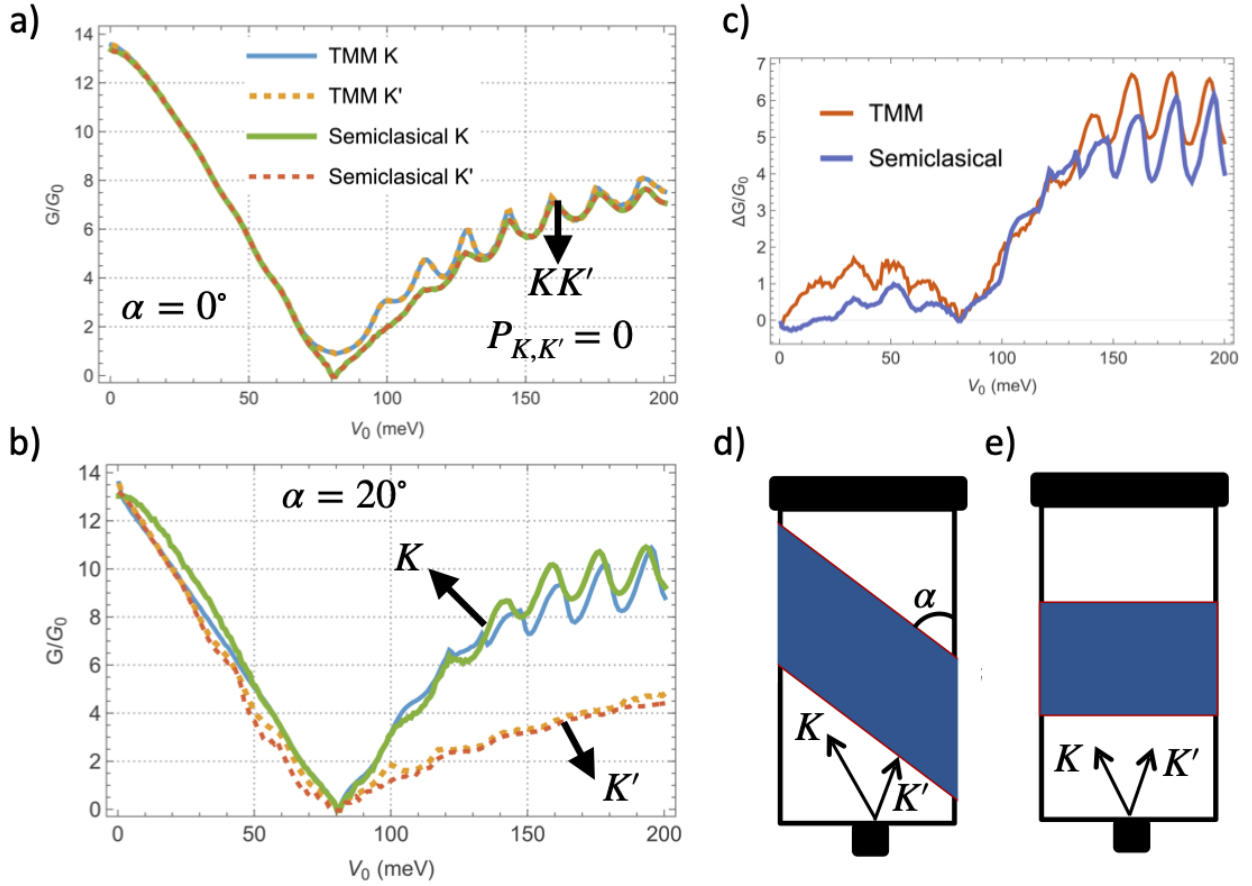


Figure 2: Valley-resolved conductance as a function of barrier height V_0 . (a) Straight barrier ($\alpha = 0^\circ$), with the device geometry illustrated in (e): G_K and $G_{K'}$ calculated by the transfer matrix method (TMM; K : blue solid, K' : orange dashed) and the semiclassical approach (K : green solid, K' : red dashed), confirming zero valley polarization ($P_{K,K'} = 0$). (b) Tilted barrier ($\alpha = 20^\circ$), with the device geometry illustrated in (d): above $V_0 \approx E_F = 80$ meV, K and K' conductances split clearly, demonstrating the valley filtering effect. (c) Valley-dependent conductance difference $\Delta G/G_0$ for $\alpha = 20^\circ$, showing the onset of valley polarization in the n - p - n regime. (d), (e) Device schematics for the tilted and straight barrier configurations, respectively. Parameters: $v_x/v_F = 0.86$, $v_y/v_F = 0.69$, $|w|/v_F = 0.32$, $\phi_t = 90^\circ$ (8- $Pmmn$ borophene), $W = 300$ nm, $L = 300$ nm, $d = 100$ nm, $E_F = 80$ meV.

B. Valley-polarized carrier trajectories

To demonstrate valley filtering in finite-device geometry, a semiclassical trajectory simulation is developed. While earlier works have shown that the tilt produces valley-dependent refraction at a barrier interface [35, 17, 16], the trajectory method developed here captures the full spatial dynamics and reveals that the angled barrier not only separates the two valleys in angle-space, but also actively filters them. To calculate the trajectories, at each barrier crossing, the parallel wave vector k_{\parallel} is recorded, and the coherent Fabry-Pérot transmission T_{FP} is evaluated from the sharp-barrier transfer matrix described in Sec. 4.1. This hybrid approach uses the semiclassical trajectories to capture finite-geometry effects (i.e., wall reflections, angle remapping) while retaining the quantum-mechanical transmission amplitudes from the transfer matrix. The trajectory opacity is weighted by the transmission probability, enabling direct visualization of valley-resolved

dynamics. The resultant conductance is given by

$$G_s^{\text{traj}} = G_0 \frac{W}{2\pi} \sum_i T_{\text{eff},i}(k_{y,i}; s), \frac{v_x^{\text{grp}}(k_{y,i}, s)}{v_F}, \Delta k_y, \quad (4)$$

where $T_{\text{eff},i}(k_{y,i}; s)$ is the coherent Fabry-Pérot transmission evaluated at the k_y of the i -th trajectory, and $\Delta k_y = (k_y^+ - k_y^-)/N$ is the uniform spacing over the propagating mode window of valley s . This discretization resembles the quantum Landauer integral in Eq. (3), with the transfer matrix transmission replaced by the trajectory-assigned transmission. This semiclassical approach provides a spatially resolved picture of the valley filtering mechanism and captures finite-geometry effects, such as wall-mediated carrier recycling, that are invisible to plane-wave transfer-matrix calculations. The carrier trajectories for both valleys across three configurations are shown in Fig. 3, using the same device geometry ($W = 300$ nm, $L = 300$ nm) and transport parameters ($E_F = 80$ meV, $V_0 = 160$ meV). Blue trajectories correspond to the K valley ($s = +1$) and red to K' ($s = -1$); the trajectory opacity is proportional to the transmission probability assigned at each barrier crossing. The barrier boundaries are indicated by black horizontal (or tilted) lines.

In graphene with $\alpha = 0^\circ$ [Fig. 3 (a)], the K and K' trajectories are indistinguishable (i.e., only blue is visible), which is a direct consequence of the isotropic, untilted Dirac cone. The trajectories exhibit symmetric Veselago focusing patterns [21] with diamond-shaped caustics between the two barrier interfaces, analogous to flat-lens focusing in negative-refractive-index media [21].

In borophene with $\alpha = 0^\circ$ [Fig. 3 (b)], the tilt breaks the angular symmetry of the carrier trajectories. The K carriers (blue) and K' carriers (red) refract in different transverse directions upon entering the barrier, which gives rise to an asymmetric Veselago focusing pattern — a tilted analogue of the graphene Veselago lens [21]. The K -valley caustic is deflected upward, while the K' caustic is deflected downward. However, despite this valley-dependent refraction, the straight barrier does not produce net valley filtering, since both valleys transmit with equal total weight when integrated over all incident angles. This is consistent with the zero-valley polarization shown in Fig. 2(a).

The picture changes qualitatively in Fig. 3 (c), where the barrier is tilted by $\alpha = 20^\circ$. The angled barrier (indicated by the tilted black lines) reorients the refraction geometry such that K -valley carriers (blue) encounter the barrier near the oblique Klein tunneling peak and transmit more efficiently, producing dense blue trajectories on the drain side. In contrast, K' carriers (red) approach the tilted barrier at unfavorable angles, are predominantly reflected, and appear as faint red trajectories that are largely confined to the source side. This spatial separation of the valley-resolved carrier flow clearly demonstrates the valley filtering mechanism: the tilted barrier preferentially passes K -valley carriers while blocking the K' valley.

Note that the trajectory method also reveals finite-geometry effects invisible to the plane-wave transfer-matrix calculation, such as wall-mediated carrier recycling controlled by the channel width W and barrier placement.

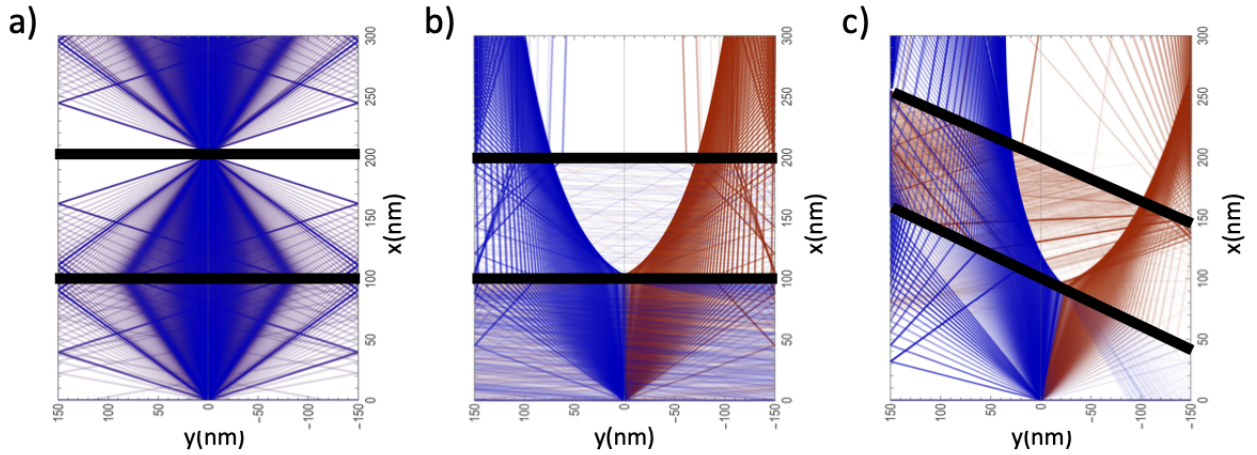


Figure 3: Semiclassical carrier trajectories from valley degeneracy to valley filtering. Each trajectory opacity is proportional to its transmission probability; blue: K ($s = +1$), red: K' ($s = -1$). Black lines indicate barrier boundaries. (a) Graphene, $\alpha = 0^\circ$: degenerate K and K' trajectories with symmetric Veselago focusing. (b) Borophene, $\alpha = 0^\circ$: the tilt induces valley-dependent refraction with asymmetric caustic patterns, but no net valley filtering. (c) Borophene, $\alpha = 20^\circ$: the tilted barrier selectively transmits K (blue) while reflecting K' (red), clearly demonstrating the valley filtering effect. Parameters: $v_x/v_F = 0.86$, $v_y/v_F = 0.69$, $|w|/v_F = 0.32$, $\phi_t = 90^\circ$ (8- $Pmmn$ borophene), $W = 300$ nm, $L = 300$ nm, $d = 100$ nm, $E_F = 80$ meV, $V_0 = 160$ meV.

C. Physical mechanism of the valley filter

The valley filtering mechanism can be understood as follows. The oblique Klein tunneling in tilted Dirac materials places the perfect-transmission directions at $+\theta_K$ and $-\theta_K$ for the K and K' valleys, respectively [15, 14]. For a straight barrier ($\alpha = 0$), the transmission profiles of the two valleys are mirror images of each other with respect to normal incidence. When integrated over all transverse modes (i.e., over all k_y), the total conductance is identical for both valleys, resulting in $P = 0$. This is the situation depicted in Fig. 1 (c) and confirmed by the valley-degenerate curves in Fig. 2 (a).

When the barrier is tilted by an angle α , the conserved quantity changes from k_y to $k_{\parallel} = k_x \sin \alpha + k_y \cos \alpha$, which effectively shifts the angular window through which carriers encounter the barrier. Crucially, this shift is the same for both valleys, but because the two valleys have their Klein tunneling peaks at opposite angles ($\pm\theta_K$), the valley-independent angular shift produces a valley-dependent change in the integrated transmission: one valley is pushed closer to its Klein tunneling peak (enhancing total transmission), while the other is pushed away (suppressing it). The filtering efficiency depends on α : as α increases from zero, it progressively breaks the valley symmetry by shifting the angular window through which each valley encounters the barrier, consequently enhancing the transmission of one valley relative to the other.

In contrast to previous valley filtering methods that utilize magnetic barriers [4, 31, 32, 33, 17] or strain engineering [7, 8, 30], the mechanism presented here is entirely electrostatic. The barrier angle α is defined lithographically, while the barrier height V_0 is tunable via gate voltage. The sign of the valley polarization is governed by the sign of α (i.e., $P(\alpha) = -P(-\alpha)$), thereby enabling geometric control over the preferred valley. The magnitude of polarization increases with V_0 in the n - p - n regime, as illustrated in Fig. 2 (b-c), which allows for continuous electrical tuning.

IV. DISCUSSION

A. Transfer matrix formalism

The coherent transmission $T(E, k_{\parallel}; s)$ is obtained from the transfer matrix formalism. In a region of constant potential V , the tilt-shifted energy is $\tilde{\varepsilon} = (E - V) - \hbar w_y s$, k_y , and the longitudinal wave-vector satisfies the quadratic equation

$$(\hbar^2 v_x^2 - \hbar^2 w_x^2 s^2) k_x^2 - 2\tilde{\varepsilon} \hbar w_x s k_x + (\hbar v_y k_y)^2 - \tilde{\varepsilon}^2 = 0, . \quad (5)$$

For pure transverse tilt ($w_x = 0$), this reduces to $k_x^2 = [\tilde{\varepsilon}^2 - (\hbar v_y k_y)^2]/(\hbar v_x)^2$. The wavefunction matrix in each region is given by

$$\Phi(x) = \begin{pmatrix} e^{ik_x x} & e^{-ik_x x} & \lambda \alpha_+ e^{ik_x x} & \lambda \alpha_- e^{-ik_x x} \end{pmatrix}, \quad (6)$$

with $\lambda = \text{sign}(\tilde{\varepsilon})$ and $\alpha_{\pm} = (\pm v_x k_x + i v_y k_y)/\sqrt{|v_x k_x|^2 + (v_y k_y)^2}$. By matching the wavefunction at the two barrier interfaces, the total transfer matrix is

$$M_{\text{total}} = \Phi^{-1} \text{free}(0), \Phi \text{bar}(0), \Phi^{-1} \text{bar}(d_{\text{eff}}), \Phi \text{free}(d_{\text{eff}}), \quad (7)$$

and the transmission probability is given by $T = 1/|[M_{\text{total}}]_{00}|^2$.

For $\alpha \neq 0$, the barrier-normal wave-vector k_{\perp} satisfies

$$A_q k_{\perp}^2 + B_q k_{\perp} + C_q = 0, \quad (8)$$

with coefficients

$$A_q = \gamma^2 - (\hbar v_x)^2 \cos^2 \alpha - (\hbar v_y)^2 \sin^2 \alpha, \quad (9)$$

$$B_q = -2\varepsilon_{\text{eff}} \gamma - 2 \sin \alpha \cos \alpha [(\hbar v_x)^2 - (\hbar v_y)^2] k_{\parallel}, \quad (10)$$

$$C_q = \varepsilon_{\text{eff}}^2 - [(\hbar v_x)^2 \sin^2 \alpha + (\hbar v_y)^2 \cos^2 \alpha] k_{\parallel}^2, \quad (11)$$

where $\gamma = \hbar w_x s \cos \alpha - \hbar w_y s \sin \alpha$ and $\varepsilon_{\text{eff}} = (E - V) - \hbar w_x s k_{\parallel} \sin \alpha - \hbar w_y s k_{\parallel} \cos \alpha$. The physically correct root requires positive group velocity along the barrier normal; a negative discriminant indicates total internal reflection. Note that these coefficients reduce to the standard expressions for the straight barrier ($\alpha = 0$) case [14, 15]. The key feature of Eqs. (9)–(11) is that the barrier angle α couples to the tilt through γ and to the anisotropy through the $\sin \alpha \cos \alpha$ cross-terms, which gives rise to the valley-dependent filtering mechanism described in this work.

B. Semiclassical equations of motion

In this approach, the sharp rectangular barrier is replaced by a smooth potential profile

$$V(x_{\text{eff}}) = \frac{V_0}{2} \left[\tanh\left(\frac{x_{\text{eff}}}{\sigma}\right) - \tanh\left(\frac{x_{\text{eff}} - d}{\sigma}\right) \right], \quad (12)$$

where σ is a small smoothing length that regularizes the step-function discontinuity, providing a continuous force gradient for the numerical integration. The smoothing length σ is chosen to be much smaller than all physical length scales ($\sigma \ll d$), so that the potential profile closely approximates the sharp barrier used in the transfer matrix calculation, where the carriers are injected from the source and propagated through the device via the semiclassical equations of motion

$$\dot{x} = w_x s v_F + \lambda v_F v_x^2 k_x / \tilde{k}, \quad (13)$$

$$\dot{y} = w_y s v_F + \lambda v_F v_y^2 k_y / \tilde{k}, \quad (14)$$

$$\hbar \dot{k}_x = -\partial V / \partial x, \quad \hbar \dot{k}_y = -\partial V / \partial y, \quad (15)$$

where $\tilde{k} = \sqrt{(v_x k_x)^2 + (v_y k_y)^2}$. The equations of motion is calculated using a fourth-order Runge–Kutta method with time step $\Delta t = 0.02$ fs. The smooth potential in Eq. (12) provides the continuous forces $-\partial V / \partial x$ and $-\partial V / \partial y = \tan \alpha; dV / dx_{\text{eff}}$ that steer the carrier momentum as it traverses the barrier. Specular reflection is imposed at the channel walls ($y = \pm W/2$).

C. *Experimental prospects*

The valley filtering mechanism described here relies on two generic ingredients: i) a tilted anisotropic Dirac cone that produces valley-split oblique Klein tunneling, and ii) an angled electrostatic barrier that converts this angular splitting into a net valley-dependent conductance. These ingredients are not specific to a single material; the framework applies to any 2D system hosting type-I tilted Dirac or Weyl cones with sufficiently large oblique Klein tunneling angle θ_K .

From the practical point of view, WTe₂ is particularly accessible among the candidate platforms. Although WTe₂ was initially predicted to host type-II Weyl fermions with overtilted energy dispersion [24], the type-II band structure is not robust against temperature: the Weyl nodes begin to separate above approximately 70 K, and a small gap of ~ 2 meV emerges around 130 K while the highly tilted, anisotropic low-energy dispersion is preserved [26]. Photothermoelectric transport measurements at room temperature have confirmed that this anisotropic transport survives well above cryogenic conditions [27]. Combined with the high carrier mobility established in this material [25], WTe₂ nanoflake devices with lithographically defined electrodes have already been fabricated and characterized [27], so cryogenic operation is not required.

A concrete experimental path can be envisioned: a WTe₂ nanoflake device with source and drain electrodes is equipped with an angled top gate that creates an *n-p-n* barrier tilted by angle α relative to the current flow direction. Valley polarization could be detected through non-local voltage measurements or through the valley-dependent Fabry–Pérot oscillation pattern in $G(V_0)$, which provides a distinctive spectroscopic fingerprint of valley filtering.

The framework is not restricted to WTe₂. The organic conductor α -(BEDT-TTF)₂I₃ possesses a stronger tilt ($\eta^2 \approx 0.53$), which may yield even stronger valley polarization. 8-*Pmmn* borophene, whose parameters are used in the calculations presented above, has been synthesized on Ag(111) [10, 23], though its transport characterization remains an experimental challenge due to substrate hybridization effects. The present calculations assume ballistic transport and a sharp

rectangular barrier profile; in practice, disorder scattering, finite-temperature phonon contributions, and smooth gate-defined potentials may modify the quantitative magnitude of the valley polarization. However, the underlying mechanism, i.e., the interplay between oblique Klein tunneling and the geometric symmetry breaking induced by the angled barrier, is robust to these effects, as it relies on the oppositely tilted Fermi-surface topology.

V. CONCLUSION

In summary, we showed that an angled electrostatic gate on a tilted Dirac material provides a purely electrostatic route to valley filtering in n - p - n junctions, without the need for magnetic fields or strain engineering. We developed a generalized transfer-matrix formalism for the tilted, anisotropic Dirac Hamiltonian, extended to treat barriers at arbitrary angles α to the transport direction, and derived the refraction equation in the rotated-barrier frame with anisotropic coefficients. The valley-resolved Landauer–Buttiker conductance of 8- $Pmmn$ borophene n - p - n junctions shows that, for $\alpha = 0$, the K and K' conductances are degenerate, whereas for $\alpha = 20^\circ$ a clear valley-dependent conductance splitting emerges in the n - p - n regime. A semiclassical trajectory simulation in the full 2D device geometry directly demonstrates that the angled barrier achieves valley filtering via a general mechanism: it relies on the interplay between valley-dependent tunneling probability and the geometric symmetry breaking introduced by the angled barrier, which is present in any type-I tilted Dirac/Weyl systems. Among the candidate materials, WTe_2 is particularly promising because it exhibits the requisite anisotropic energy dispersion at room temperature [26, 27]. In the proposed scheme, the device parameters can be further optimized to achieve higher valley polarization, and the framework may pave the way for experimental realization of all-electrostatic valley filters in the growing family of materials hosting tilted Dirac and Weyl cones. This work demonstrates that purely electrostatic valley filtering is not only theoretically robust, but also experimentally feasible, providing a clear pathway for realizing all-electrostatic valley filter devices.

VI. ACKNOWLEDGMENTS

The author acknowledges the support of the Nanoelectronics Research Center (Nano Electronics Research Mühendislik Ar. Ge. Ltd. Şti. Istanbul Turkey).

VII. DATA AVAILABILITY

The data are available from the corresponding author upon reasonable request.

VIII. CODE AVAILABILITY

The semiclassical transport simulator used in this work is available from the corresponding author upon reasonable request.

IX. AUTHOR CONTRIBUTIONS

C.Y. conceived the idea, developed the theoretical framework, performed all calculations, and wrote the manuscript.

X. COMPETING INTERESTS

The author declares no competing interests.

REFERENCES

- [1] A. Rycerz, J. Tworzydło, and C. W. J. Beenakker, Valley filter and valley valve in graphene. *Nat. Phys.* **3**, 172–175 (2007).
- [2] D. Xiao, W. Yao, and Q. Niu, Valley-contrasting physics in graphene: Magnetic moment and topological transport. *Phys. Rev. Lett.* **99**, 236809 (2007).
- [3] J. R. Schaibley *et al.*, Valleytronics in 2D materials. *Nat. Rev. Mater.* **1**, 16055 (2016).
- [4] M. Settnes, S. R. Power, M. Brandbyge, and A.-P. Jauho, Graphene nanobubbles as valley filters and beam splitters. *Phys. Rev. Lett.* **117**, 276801 (2016).
- [5] J. R. Williams and C. M. Marcus, Snake states along graphene p - n junctions. *Phys. Rev. Lett.* **107**, 046602 (2011).
- [6] T. Taychatanapat *et al.*, Conductance oscillations induced by ballistic snake states in a graphene heterojunction. *Nat. Commun.* **6**, 6093 (2015).
- [7] F. Guinea, M. I. Katsnelson, and A. K. Geim, Energy gaps and a zero-field quantum Hall effect in graphene by strain engineering. *Nat. Phys.* **6**, 30–33 (2010).
- [8] N. Levy *et al.*, Strain-induced pseudo-magnetic fields greater than 300 tesla in graphene nanobubbles. *Science* **329**, 544–547 (2010).
- [9] A. Lopez-Bezanilla and P. B. Littlewood, Electronic properties of 8- $Pmmn$ borophene. *Phys. Rev. B* **93**, 241405(R) (2016).
- [10] B. Feng *et al.*, Dirac fermions in borophene. *Phys. Rev. Lett.* **118**, 096401 (2017).
- [11] A. D. Zabolotskiy and Y. E. Lozovik, Strain-induced pseudomagnetic field in the Dirac semimetal borophene. *Phys. Rev. B* **94**, 165403 (2016).
- [12] M. O. Goerbig, J.-N. Fuchs, G. Montambaux, and F. Piéchon, Tilted anisotropic Dirac cones in quinoid-type graphene and α -(BEDT-TTF)₂I₃. *Phys. Rev. B* **78**, 045415 (2008).
- [13] T. E. O’Brien, M. Diez, and C. W. J. Beenakker, Magnetic breakdown and Klein tunneling in a type-II Weyl semimetal. *Phys. Rev. Lett.* **116**, 236401 (2016).

- [14] Z. Kong, J. Li, Y. Zhang, S.-H. Zhang, and J.-J. Zhu, Oblique and asymmetric Klein tunneling across smooth NP junctions or NPN junctions in 8-*Pmmn* borophene. *Nanomaterials* **11**, 1462 (2021).
- [15] S.-H. Zhang and W. Yang, Oblique Klein tunneling in 8-*Pmmn* borophene *p-n* junctions. *Phys. Rev. B* **97**, 235440 (2018).
- [16] V. H. Nguyen and J.-C. Charlier, Klein tunneling and electron optics in Dirac-Weyl fermion systems with tilted energy dispersion. *Phys. Rev. B* **97**, 235113 (2018).
- [17] C. Yesilyurt, S. G. Tan, G. Liang, and M. B. A. Jalil, Electrically tunable valley polarization in Weyl semimetals with tilted energy dispersion. *Sci. Rep.* **9**, 4461 (2019).
- [18] S.-H. Zhang, W. Yang, and F. M. Peeters, Veselago focusing of anisotropic massless Dirac fermions. *Phys. Rev. B* **97**, 205437 (2018).
- [19] M. A. Mojarro, R. Carrillo-Bastos, and J. A. Maytorena, Resonant transport and line-type resonances in tilted Dirac cone double-barrier structures. *arXiv:2508.17220* (2025).
- [20] S.-H. Zhang, D.-F. Shao, Z.-A. Wang, J. Yang, C.-Y. Yang, and E. Y. Tsymbal, Tunneling valley Hall effect driven by tilted Dirac fermions. *Phys. Rev. Lett.* **131**, 246301 (2023).
- [21] V. V. Cheianov, V. Fal'ko, and B. L. Altshuler, The focusing of electron flow and a Veselago lens in graphene *p-n* junctions. *Science* **315**, 1252–1255 (2007).
- [22] P. E. Allain and J. N. Fuchs, Klein tunneling in graphene: optics with massless electrons. *Eur. Phys. J. B* **83**, 301–317 (2011).
- [23] A. J. Mannix *et al.*, Synthesis of borophenes: anisotropic, two-dimensional boron polymorphs. *Science* **350**, 1513–1516 (2015).
- [24] A. A. Soluyanov, D. Gresch, Z. Wang, Q. Wu, M. Troyer, X. Dai, and B. A. Bernevig, Type-II Weyl semimetals. *Nature* **527**, 495–498 (2015).
- [25] M. N. Ali *et al.*, Large, non-saturating magnetoresistance in WTe_2 . *Nature* **514**, 205–208 (2014).
- [26] Y.-Y. Lv *et al.*, Experimental observation of anisotropic Adler-Bell-Jackiw anomaly in type-II Weyl semimetal $\text{WTe}_{1.98}$ crystals at the quasiclassical regime. *Phys. Rev. Lett.* **118**, 096603 (2017).
- [27] Q. Wang, C. Yesilyurt, F. Liu, Z. B. Siu, K. Cai, D. Kumar, Z. Liu, M. B. A. Jalil, and H. Yang, Anomalous photothermoelectric transport due to anisotropic energy dispersion in WTe_2 . *Nano Lett.* **19**, 2647–2652 (2019).
- [28] K. F. Mak, K. He, J. Shan, and T. F. Heinz, Control of valley polarization in monolayer MoS_2 by optical helicity. *Nat. Nanotechnol.* **7**, 494–498 (2012).

- [29] D. Gunlycke and C. T. White, Graphene valley filter using a line defect. *Phys. Rev. Lett.* **106**, 136806 (2011).
- [30] V. M. Pereira and A. H. Castro Neto, Strain engineering of graphene's electronic structure. *Phys. Rev. Lett.* **103**, 046801 (2009).
- [31] T. Fujita, M. B. A. Jalil, and S. G. Tan, Valley filter in strain engineered graphene. *Appl. Phys. Lett.* **97**, 043508 (2010).
- [32] C. Yesilyurt, S. G. Tan, G. Liang, and M. B. A. Jalil, Efficient dual spin-valley filter in strained silicene. *Appl. Phys. Express* **8**, 105201 (2015).
- [33] C. Yesilyurt, S. G. Tan, G. C. Liang, and M. B. A. Jalil, Perfect valley filter in strained graphene with single barrier region. *AIP Advances* **6**, 056303 (2016).
- [34] F. Zhai, X. Zhao, K. Chang, and H. Q. Xu, Magnetic barrier on strained graphene: A possible valley filter. *Phys. Rev. B* **82**, 115442 (2010).
- [35] C. Yesilyurt *et al.*, Anomalous tunneling characteristic of Weyl semimetals with tilted energy dispersion. *Appl. Phys. Lett.* **111**, 063101 (2017).
- [36] C. Yesilyurt, Z. B. Siu, S. G. Tan, G. Liang, and M. B. A. Jalil, Conductance modulation in Weyl semimetals with tilted energy dispersion without a band gap. *J. Appl. Phys.* **121**, 244303 (2017).
- [37] C. Yesilyurt, S. G. Tan, G. Liang, and M. B. A. Jalil, Klein tunneling in Weyl semimetals under the influence of magnetic field. *Sci. Rep.* **6**, 38862 (2016).